Slab to back-arc to arc: fluid and melt pathways through the mantle wedge beneath the Lesser Antilles

Stephen P. Hicks[1], Lidong Bie[2], Catherine A. Rychert[3], Nicholas Harmon[3], Saskia Goes[1], Andreas Rietbrock[4], Songqiao Shawn Wei[5], Jenny S. Collier[1], Timothy J. Henstock[3], Lloyd Lynch[6], Julie Prytulak[7], Colin Macpherson[7], David Schlaphorst[8], Jamie J. Wilkinson[9], Jonathan D. Blundy[10], George F. Cooper[11], John-Michael Kendall[10].

1. Department of Earth Science & Engineering, Imperial College London
2. School of Environmental Sciences, University of East Anglia
3. School of Ocean and Earth Science, University of Southampton
4. Karlsruhe Institute of Technology
5. Department of Earth and Environmental Sciences, Michigan State University
6. Seismic Research Centre, The University of the West Indies
7. Department of Earth Sciences, Durham University
8. Instituto Dom Luiz, University of Lisbon
9. London Natural History Museum
10. Department of Earth Sciences, University of Oxford
11. School of Earth and Ocean Sciences, Cardiff University

Corresponding author: Stephen P. Hicks (email: s.hicks@imperial.ac.uk)

Abstract

Volatiles expelled from subducted plates melt the overlying warm mantle, feeding arc volcanism. However, debates continue over the factors controlling melt generation and transport and how these determine the placement of volcanoes. To broaden our synoptic view of these fundamental mantle wedge processes, we image seismic attenuation beneath the Lesser Antilles arc, an end-member system that slowly subducts old, tectonised lithosphere. Punctuated anomalies with high ratios of bulk-to-shear attenuation (Q_κ^{-1}/Q_μ^{-1} > 0.6) and V_P/V_S (>1.83) lie 40 km above the slab, representing expelled fluids that are retained in a cold boundary layer, transporting fluids towards the back-arc. The strongest attenuation ($1000/Q_S$~20), characterising melt in warm mantle, lies beneath the back-arc, revealing how back-arc mantle feeds arc volcanoes. Melt ponds under the upper plate and percolates toward the arc along structures from earlier back-arc spreading, demonstrating how slab dehydration, upper plate properties, past tectonics, and resulting melt pathways collectively condition volcanism.

1 Introduction

By delivering volatiles to the deep Earth and returning them to the surface, subduction zones are a key player in Earth's deep water cycle. This volatile cycling generates earthquakes and ore deposits and causes the mantle to melt, which leads to potentially hazardous volcanic eruptions. Magmatism in subduction zones occurs along volcanic arcs and back-arc spreading centres. For volcanic arcs, expelled volatiles from subducting slabs lower the solidus temperature of the mantle wedge, generating melt (*1–3*). Slab dehydration and mantle wedge melting can be modelled geodynamically and geochemically (*4–8*), yet the fundamental controls on melt genesis and arc position at the surface remain debated (*9*). Debates often fall into two end-member hypotheses (*9*). In the first, deep processes in the slab and mantle wedge dominate variations in magmatism, with slab devolatilisation and mantle wedge thermal structure playing key roles (*10*). In the second, upper plate controls such as stress state, pre-existing structures (*11*), and storage are most crucial. Understanding what dictates melt generation and transport and determines the location of volcanoes is vital for fully understanding hazardous subduction zone systems.

A key factor driving flux melting is the thermal structure of the slab and mantle wedge. Temperature is governed mainly by the age and velocity of the downgoing lithosphere, as well as the depth where the slab and mantle couple mechanically (*12*, *13*). In numerical models, there is a sharp coupling transition depth (hereafter CTD; also called 'decoupling depth') at ~80 km (*6*, *14*). Many models assume that volatiles and melt rise vertically because of their positive buoyancy (*5*, *6*, *15–17*); slab surface temperatures inferred by some geothermometry data broadly support such assumptions (*18*). However, when considering compaction effects, some models show more complex fluid and melt pathways through the mantle (*7*, *8*), with a likely impact on magma genesis and arc position. Melt generation and transport depend on several other factors. These include laterally variable slab hydration (*19*), properties of the thermal boundary layer (hereafter TBL; also called 'viscous blanket') atop the slab (*7*, *20*), permeability structure along the base of the upper plate (*1*, *8*, *21–23*), and long-term arc migration (*24*). It is vital to constrain such models with observations.

Intrinsic seismic attenuation, expressed by the inverse quality factor, Q^{-1}, is sensitive to temperature and melt (*25*), offering a window into critical geodynamic processes beneath

volcanic arcs. Images of Q^{-1} offer insights into slab dehydration (*26*), melt generation (*27*), transport mechanisms (*28*) and their relationship to volcanic output (*26*, *29*, *30*). Jointly imaging bulk and shear attenuation (Q_κ^{-1} and Q_μ^{-1}) can distinguish the free fluids from melt. For example, a high Q_κ^{-1}/Q_μ^{-1} ratio (>0.8) in a low Q_μ^{-1} medium indicates thermoelastic relaxation due to fluid pockets enhancing grain-scale heterogeneity (*28*, *30*, *31*).

Previous Q^{-1} tomography studies focussed on Pacific-type subduction zones, which generally subduct plates predominantly formed at intermediate-to-fast-spreading ridges at a relatively high rate (>4 cm/yr). Tomographic images typically show a sharp lateral transition spanning less than 50 km, from low Q^{-1} in the rigid cold nose in the fore-arc corner to high Q^{-1} of the warm convecting mantle, representing a sharp slab-mantle CTD (*12*) that numerical models predict (*6*). Apart from regions with active back-arc spreading, such as Tonga-Lau (*28*), the highest Q^{-1} typically lies directly beneath the volcanic front, at 50-100 km depth (*26–30*, *32–34*). These Q^{-1} anomalies typically overlap with a region of high V_P/V_S (>1.8) (*35–37*). To first-order, these sub-arc seismic anomalies reinforce the classic paradigm that once melt is generated, it takes a mostly vertical path to the arc above. However, thermal structure and slab devolatilisation depend on plate age and subduction velocity (*6*), along with hydration of the incoming plate being influenced by the spreading rate at its formation (*19*). Therefore, our understanding of fundamental mantle wedge processes may be biased by Pacific-type subduction systems.

To account for the global diversity in subduction systems, this study focuses on the end-member Lesser Antilles Arc (LAA) subduction system (Figure 1) due to its slow consumption (~19 mm/yr) of old (80-120 Ma), slow-spread lithosphere. The sub-arc slab depth for the north-central LAA is ~120-140 km (*38*), deeper than the global average of 105 km (*13*), which might hint at a ~70-90 km thick zone of convecting sub-arc mantle, yet it is largely isotropic based on *S*-wave splitting (*39*). The narrow zone of volcanism (Figure 1) provides an opportunity to image and infer fundamental melt pathways through the mantle.

Past tectonics in the Eastern Caribbean may impact present-day melt pathways through the upper plate. The frontal volcanic arc on the overriding Caribbean plate stepped backwards at 40 Ma and then forward, to its current position, at 20 Ma (*40*), which may have left relic pathways for present-day melt transport pathways. Back-arc spreading accompanied these previous arcs, but there is no evidence for rifting in the Grenada Basin today (*40*).

There are also lateral variations in the hydration state of the oceanic lithosphere before its subduction into the Antilles trench. Seismic images reveal a heterogeneous incoming plate with alternating tectonised and magmatically-robust segments (*41*). During outer rise bending at the Antilles trench, overall hydration increases whilst preserving its original spatial pattern (Allen et al., in press, JGR). In addition, there is evidence for variable hydration within the subducted slab. The highest rate of intra-slab, intermediate-depth earthquakes (maximum depth of nearly 200 km) occurs in a narrow region between Martinique and Dominica (*38*). Seismicity *b*-values peak offshore Martinique (*42*). Seismic velocities imaged using local earthquakes show dehydration of slab crust and serpentinised mantle at ~60 and ~150 km depth, respectively (*43*). Serpentine-derived fluids identified using boron isotopes (*19*) imply unusually high degrees of mantle hydration along the Marathon and Mercurius FZs (Figure 1), representing the boundary between the Proto-Caribbean and Equatorial Atlantic oceanic domains (*44*). Tomographic imaging and receiver functions (*45–48*) show along-arc variations in *S*-wave velocity (V_S), with the slowest segment of upper plate mantle and mantle wedge lying beneath Dominica and extending 100 km into the back-arc.

Crucial unanswered questions remain about the LAA. Notably, why are low V_S anomalies in the back-arc mantle wedge are offset from FZs, and why there is no high V_P/V_S in the sub-arc mantle wedge (*43*, *45*) as seen beneath Pacific arcs? To address these questions, this study investigates the locations and mechanisms of flux melting in the mantle wedge and the resultant melt pathways beneath the LAA. The LAA provides a unique opportunity to examine the effects of an end-member subduction system and long-term arc migration. However, the largely submarine nature of ocean-ocean subduction zones presents a challenge in imaging the mantle wedge. In this study, we use seismic data from a temporary ocean-bottom seismometer (OBS) network in the LAA (*49*) that, combined with on-island arc stations, offers robust imaging of the slab, mantle, and upper plate. We focus on the most seismically active segment of the arc, from Martinique to Montserrat (Figure 1). We compute the whole-path attenuation operator, t^*, for ~2,500 *P*- and *S*-waves to tomographically invert for the 2-D and 3-D variation of Q^{-1} (see *Methods and Materials*). After thorough tests of model resolution, we interpret substantial variations in Q^{-1} perpendicular to and along the arc. We combine our Q^{-1} models with previously published seismic velocities and compare Q against theoretical predictions from geodynamic models to interpret pathways of partial melts and slab-derived volatiles and melt through the mantle wedge beneath the LAA.

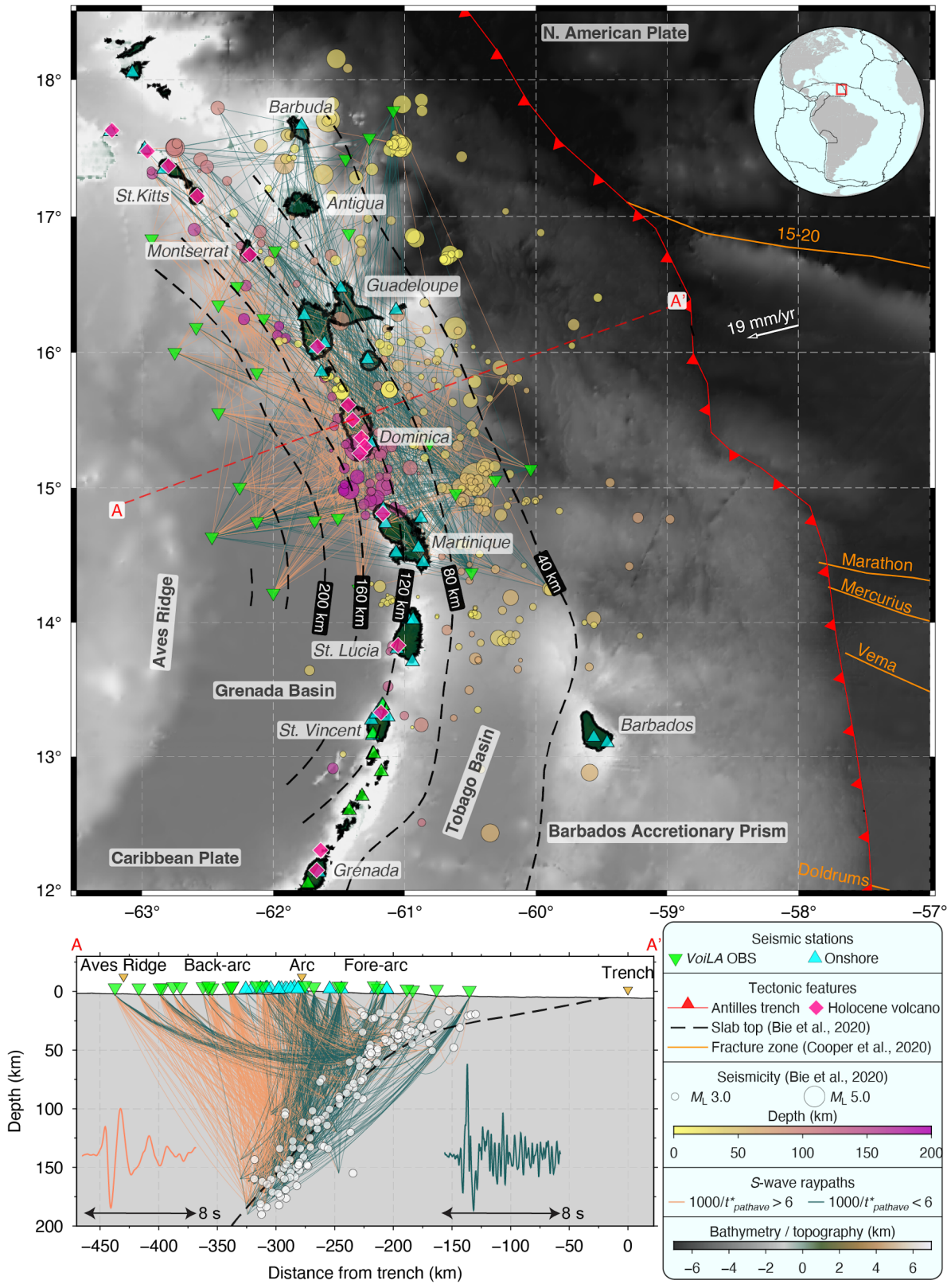

Figure 1. Seismotectonic context of the Lesser Antilles arc, with *S*-wave raypath coverage and path-averaged t^*_S results. The red box on the inset map shows the extent of the main map. Island names are labelled in italic; tectonic features are in bold. Raypaths in the map (top) and cross-section view (bottom) are traced in a 3-D velocity model (*43*), with colours showing path-averaged t^*. Orange paths have strong attenuation; green have weak attenuation. The location of Section *A*-*A*' is marked by the red dashed line on the map. Representative 8-second-long *S*-wave waveforms (transverse component) are given for back-arc raypaths (orange) and a fore-arc path (green) from the same intra-slab earthquake at 180 km depth (details in Figure S5).

2 Spatial variability in seismic attenuation

P- and *S*-waveforms from intraslab earthquakes at intermediate depth recorded on OBS stations in the back-arc show substantial high-frequency attenuation (Figure S5). We verify this initial result by visualising path-averaged t^* values for each raypath (Figure 1). In contrast, weakly attenuating raypaths are those that travel up through the slab and fore-arc. Within the constraints of our resolution tests and assumptions in our t^* spectral fitting method, we describe a 2-D and more detailed 3-D seismic attenuation model for the LAA using a 3-D velocity model (*43*). Our tests show that the shape and amplitude of the main attenuation anomalies are insensitive to assumptions about station corrections and corner frequency. We can resolve anomalies with characteristic lengths of 25-50 km under the fore-arc, arc, and back-arc (see *Methods and Materials* for full details).

Our tomographic inversions for Q^{-1} reveal considerable *P*- and *S*-wave attenuation variations perpendicular and parallel to the LAA. We identify the first-order components of the LAA Q^{-1} structure from the 2-D inversion (Figure 2) within the framework of structural boundaries from previous work. In particular: the upper plate Moho (*50*), the slab top inferred from seismicity (*38*), and the upper plate lithosphere-asthenosphere boundary (LAB) (*47*) (Figure 2). Notably, the most prominent Q^{-1} anomalies do not directly correspond to V_P or V_P/V_S anomalies, suggesting that the physical properties responsible for these different types of seismic anomalies are spatially decoupled. We present the 3-D tomographic model in arc-perpendicular and depth sections in Figures 3 and 4, respectively. Given the more substantial *S*-wave attenuation, we present Q_S^{-1} and Q_κ^{-1}/Q_μ^{-1} ratio in 3-D. We identify the main features described below.

Subducting oceanic lithosphere ('sol'). We find the lowest Q^{-1} in the subducted slab ($1000/Q < 4$), which is present across the arc and is consistent with variations in slab geometry (*38*).

fore-arc mantle corner ('fmc'). Like the slab, the fore-arc mantle is weakly attenuating ($1000/Q_S < 4$). The mantle corner appears as a large, uniformly low Q_S^{-1} anomaly beneath the fore-arc and volcanic arc, extending from the upper plate Moho at 30 km depth to the top of the subducting plate at 120 km depth (Figure 2). In 3-D, the low Q_S^{-1} fore-arc mantle corner appears persistent throughout the arc; however, its appearance varies subtly. Beneath Martinique (section D-D'), the fore-arc corner is more prominent and has a sharper,

near-vertical boundary with the back-arc mantle wedge (Figure 3). Whereas further north beneath Guadeloupe (section B-B'), the fore-arc corner anomaly is smaller and has a weaker contrast with the mantle wedge. Although relatively non-attenuating, the fore-arc mantle displays a high Q_κ^{-1}/Q_μ^{-1} (>0.6). In the arc-parallel profile (Figure 3, section E-E'), this high Q_κ^{-1}/Q_μ^{-1} anomaly has a punctuated appearance, being most prominent directly beneath the islands, especially Guadeloupe and Dominica.

Mantle wedge asthenosphere ('mw'). Below the back-arc, there is a sharp increase in Q^{-1} at depths greater than 60 km. We see the most prominent, highest Q_P^{-1} and Q_S^{-1} anomalies ($1000/Q$ > 20) at depths of 60–140 km and, unexpectedly, 40-70 km west of the volcanic arc, which we interpret as the asthenospheric mantle (Figure 2). The high Q^{-1} does not seem to extend to the top of the slab, lying ~40 km above it. Throughout the back-arc, the high Q_S^{-1} mantle wedge extends up to the upper plate LAB, where there is a strong Q^{-1} gradient. This attenuating wedge extends into the back-arc 100 km west of the volcanic arc, at least to the westernmost limit of our resolution. Although a high Q_S^{-1} asthenosphere wedge feature appears throughout the LAA, our 3-D inversion (Figures 3-4) suggests two possibly distinct mantle wedge anomalies (labelled '*mw1*' and '*mw2*'). The highest Q_S^{-1} values in the asthenosphere wedge ($1000/Q_S$ = 17-25) lie at 80-110 km depth beneath the back-arc of Dominica (*mw1*) (section C-C'). South of *mw1*, wedge Q^{-1} rapidly decreases ($1000/Q_S$ = 7-9) beneath Martinique (section D-D'). To the north, between Guadeloupe and Montserrat (sections A-A' and B-B'), a more muted high Q_S^{-1} ($1000/Q_S$=11-14; '*mw2*') extends to shallower depths of 50 km. Compared to the fore-arc corner, the back-arc mantle wedge has a more moderate Q_κ^{-1}/Q_μ^{-1} (0.4-0.6), suggesting almost negligible bulk attenuation.

Overriding Caribbean lithosphere ('ocl'). Our resolution tests show lateral and vertical smearing between nodes at shallow depths (<40 km). Nevertheless, we tentatively identify low Q^{-1} ($1000/Q_S$ = 4–8) sandwiched between the LAB (*47*) and Moho, and a shallower high Q^{-1} ($1000/Q_S$ = 8–12), which is clearest in the 2-D Q_S^{-1} model, where it extends from the arc to up to ~50 km west into the back-arc (Figure 2). We do not have the resolution to determine how this anomaly varies beneath the different islands (Figures 3-4).

Synthetic tests

To better understand the robustness of our identified features, we designed a set of synthetic models around some critical questions. (a) Can we resolve a high Q^{-1} mantle wedge

under the fore-arc that would be more consistent with a CTD of 80 km based on Pacific studies? (b) Can our inversion distinguish a high Q^{-1} mantle wedge from a high Q^{-1} in the sub-arc crust? (c) Can we successfully resolve the geometry of a high Q^{-1} mantle wedge beneath the back-arc and (d) image along-arc variations in its amplitude? Figure 5 shows the synthetic models with labelled anomalies corresponding to the questions above. Similar to our checkerboard tests (see *Methods and Materials*), we computed corresponding synthetic t^* measurements, added noise to the data, and inverted these data, as per our actual data inversions.

The resulting inversions (Figure 5) recover the long-wavelength shapes and the absolute Q^{-1} values of many input anomalies. In particular, our results show that the high Q^{-1} anomaly in the sub-arc crust (b) is resolvable. We can rule out the possibility of a localised high Q^{-1} anomaly in the fore-arc mantle wedge that would indicate a CTD at ~80 km depth (a). We can also distinguish mantle wedge structures from high Q^{-1} anomalies in the upper plate (c). Finally, the geometry and amplitude of the high Q^{-1} back-arc mantle wedge (d), with its along-arc peak near Dominica, are robust.

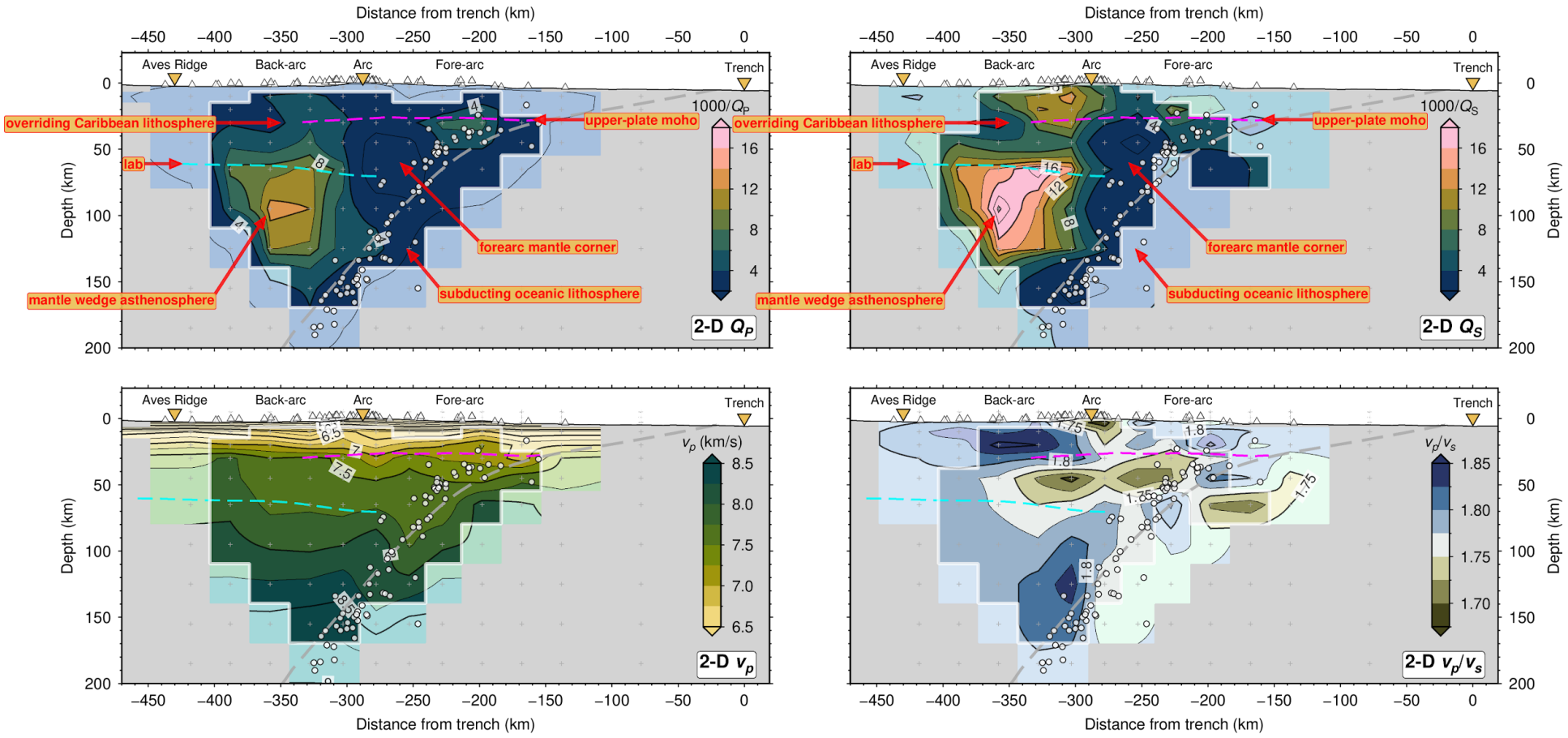

Figure 2. 2-D *P*-wave (top-left) and *S*-wave (top-right) Q^{-1} models compared with 2-D *P*-wave velocity (bottom-left) and V_P/V_S ratio (bottom-right) (*43*). The magenta dashed line indicates the upper plate Moho (*50*). The dashed cyan line indicates a negative seismic velocity discontinuity interpreted as the lithosphere-asthenosphere boundary (LAB) at the base of the Caribbean plate (*47*). White plus symbols indicate the model inversion nodes. White circles are event hypocentres; white triangles are stations. The cross-section corresponds to the A-A' shown in Figure 3. The white line surrounding the most opaque colours denotes the resolution limit from Figure S6a.

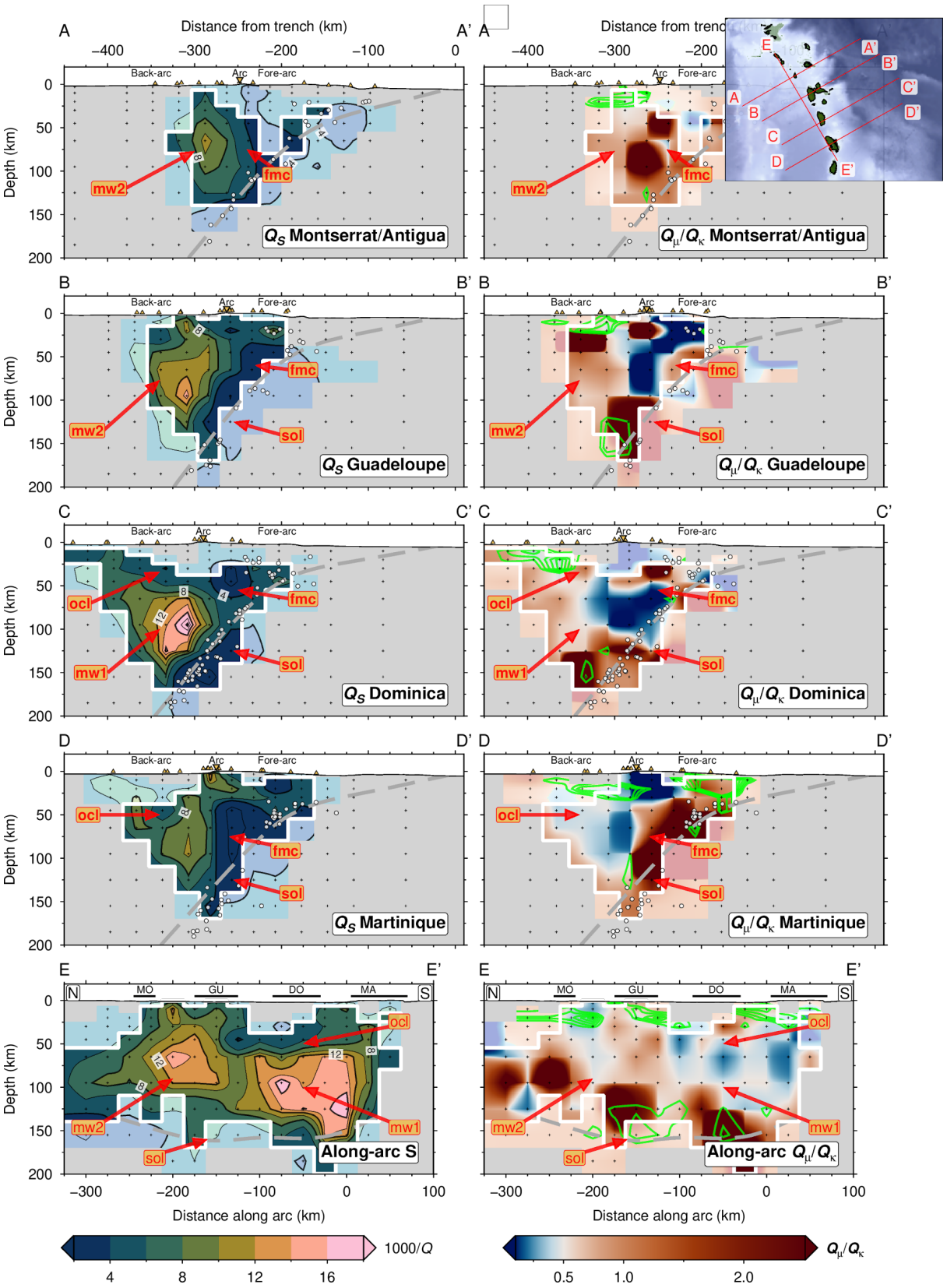

Figure 3. Cross-sections through the 3-D Q_S^{-1} (left) and Q_μ/Q_κ (right) models. The inset map (top-right) shows the location of each section. The top four rows (A-A' to D-D') are arc-perpendicular; the bottom row (E-E') is an arc-parallel section in the back-arc, with the labelled horizontal black lines showing the extent of islands at the surface (MO=Montserrat; GU=Guadeloupe; DO=Dominica; MO=Martinique). The green contours on the Q_μ/Q_κ images denote zones of high V_P/V_S (>1.83; intervals of 0.01) (*43*). The grey dashed line is the slab interface. Labelled features (fmc = fore-arc mantle corner; mw = mantle wedge; clm = Caribbean lithosphere mantle; sal = subducting Atlantic lithosphere) are discussed in the text.

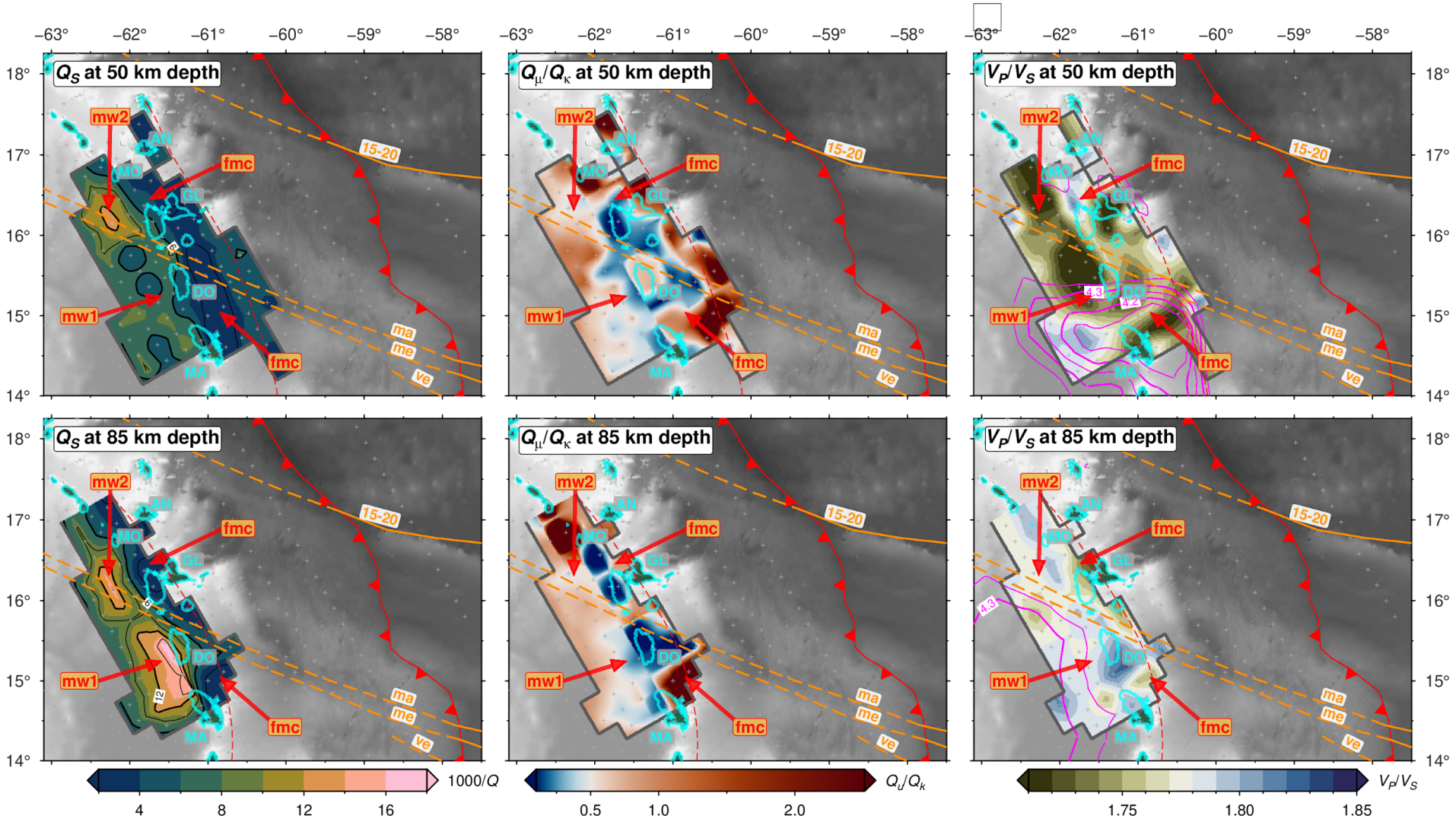

Figure 4. Tomographic images through the 3-D model in map view. Attenuation is presented at depths of 50 km (top row) and 85 km (bottom row), showing Q_S^{-1} (left) and Q_μ/Q_κ (middle), and V_P/V_S (right) (*43*) and V_S from teleseismic rayleigh waves (*45*). Low V_S zones are highlighted by the magenta contours covering 4.15-4.35 km/s at intervals of 0.05 km/s. The thick cyan lines give the coastlines of islands. Fracture zones (and their projected positions) are shown as (dashed) orange lines (15-20 = Fifteen-Twenty; ma = Marathon; me = Mercurius; ve = Vema). The location of the slab interface at the corresponding depth is shown by the red dashed line. Labelled features are defined as per Figure 3 and discussed in the text.

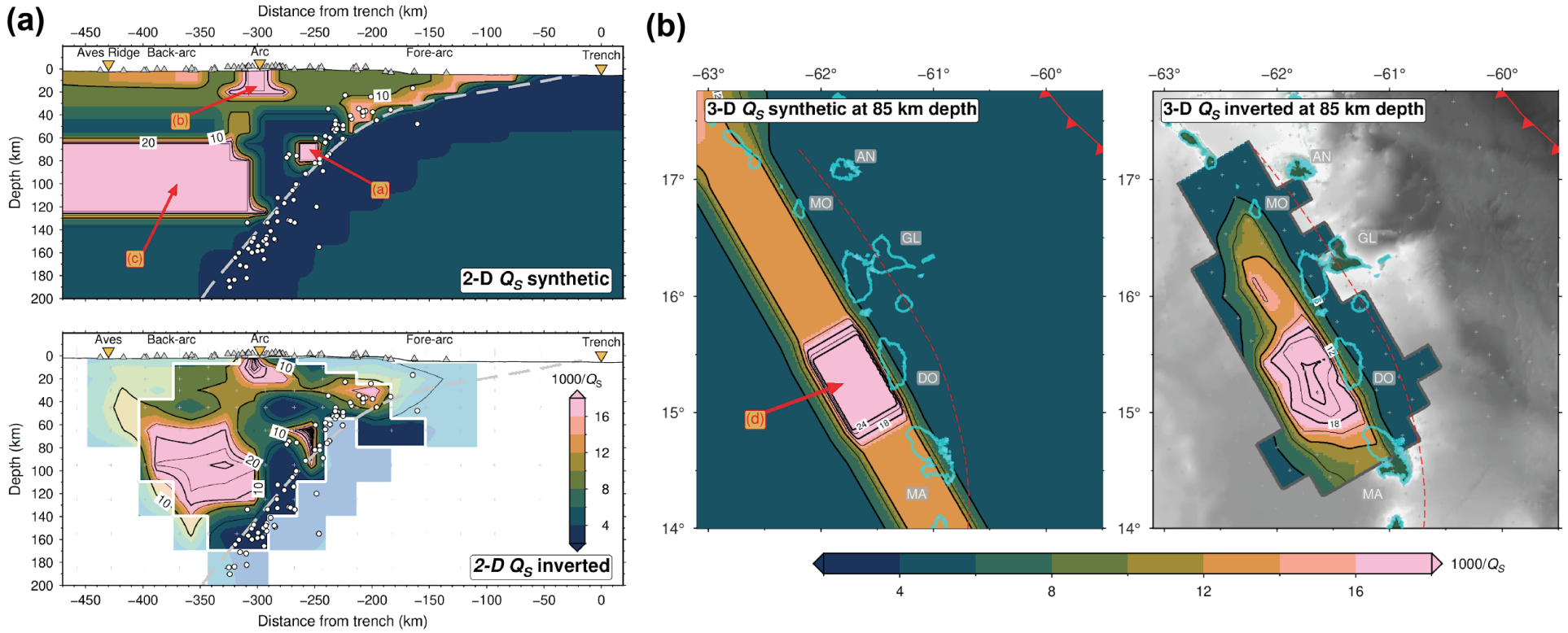

Figure 5. Restoring resolution tests. (a) Synthetic test with the 2-D inversion showing the input model (top) and the recovery (bottom). b) Similar test with the 3-D inversion to recover along-arc variability in mantle wedge attenuation with the input model (left) and the recovered model (right). Alphabetically labelled features are discussed in the text. All labelled features are present in the real model apart from (a).

3 Mantle wedge temperature, volatile pathways and melt generation

We compare the imaged seismic attenuation structure with published seismic velocity models from local earthquake tomography (V_P and V_P/V_S) (*43*, *51*) along with V_S from teleseismic Rayleigh waves (*45*) and ambient noise (*46*). Then, we interpret the most likely thermal structure, volatile and melt content, and their pathways, by using experimental and numerical geodynamic predictions as a guide (*25*, *43*, *45*, *52*, *53*). We make these interpretations within the context of the two slab dehydration pulses inferred from high V_P/V_S (>1.8) anomalies in local tomography (*43*), indicating serpentinised slab crust and mantle at 60-80 km and >120 km depth, respectively.

3.1 Volatile flux beneath the fore-arc and implications for slab-mantle coupling

The fore-arc mantle that overlies the first slab dehydration peak at 60-80 km depth with a V_P of 7.5-8.2 km/s and low-moderate V_P/V_S (<1.74) is non-attenuating across the arc ($1000/Q_S$ < 4); (Figures 2-4), indicating cold, melt-free mantle. A strong lateral gradient in Q^{-1} between this cold nose and the hot wedge is most apparent in our 2-D inversion (Figure 2). There is no similarly strong gradient in seismic velocities, which are more influenced by compositional changes, such as the presence of serpentine in cold mantle (*12*, *54*, *55*), rather than temperature. If we interpret the intersection of this boundary with the slab top in our 2-D inversion (Figure 2), we infer a CTD of 100-120 km. This value is deep compared to other subduction zones (*12* and references therein) and is inconsistent with slab crust dehydration at 60-80 km depth (*43*) because the CTD controls where the wedge rapidly heats the slab (*8*). Generally, slab crust should fully dehydrate within 20 km of the CTD (*5*), which is supported by numerical models of the LAA (*43*). Yet our 3-D inversion shows the strength of this boundary seems to vary along-strike (Figure 3), appearing sharpest under Martinique. Therefore, we suggest that the CTD may also vary along the arc or is complicated by the presence of a thick TBL atop the slab, which we discuss in the following section. Regardless of the CTD beneath the LAA, the weak local *S*-wave splitting observed at stations on the island arc (~0.2 s) (*39*) support our overall view of cold, stagnant mantle without aligned melt lying under the arc (Figure 6).

Given the low-moderate V_P/V_S of the stagnant forearc mantle corner and the age of the incoming lithosphere, the expected small fluxes of these crustal-derived volatiles do not

substantially serpentinise the fore-arc mantle thus remaining as free fluids, similar to in other cold subduction zones (*56*). This first pulse of slab dehydration thus does not directly contribute to arc magmatism via fore-arc pathways because the mantle beneath the fore-arc and arc is too cold for sourcing the primary melts that supply the arc. Many of these fluids expelled from the slab crust are likely lost in the forearc and facilitate the abundant seismicity in the fore-arc mantle of the LAA (*38*, *51*, *57*, *58*) due to raised pore fluid pressures.

3.2 Volatile flux and mantle wedge melting beneath the back-arc

The second peak of high V_P/V_S (>1.8) along the slab top lies at >140 km depth (Figure 2) and was previously interpreted as relating to fluids expelled by antigorite and chlorite dehydration in the slab mantle (*43*). However, our high Q_S^{-1} does not coincide with high V_P/V_S in the mantle wedge (Figures 2-4; Figure S12), which is different to tomographic images from other subduction zones (*26*, *29*, *35*, *36*). Instead, the high Q_S^{-1} is shifted ~10-20 km into the back-arc and ~50 km shallower, extending upwards to the overriding plate LAB at ~60 km depth (*47*). Given that the V_P/V_S (*43*) and Q^{-1} inversions use the same earthquake dataset with similar imaging resolution, this offset is real and must arise from sensitivity to different material properties, which we discuss below.

In the 40 km-thick low Q_S^{-1} zone atop the slab, there is some spatial overlap between high Q_κ^{-1}/Q_μ^{-1} (>0.6) and high V_P/V_S (>1.83) (Figure 3; Figure S12). High Q_κ^{-1}/Q_μ^{-1} in a relatively low Q_μ^{-1} medium may arise from thermoelastic relaxation attenuation caused by isolated pockets of free fluid, enhancing grain-scale heterogeneity in cold mantle (*30*, *31*). The corresponding fast seismic velocities (V_P > 8 km/s; V_{SV} > 4.45 km/s) and *k*-means clustering of seismic properties (Table S1) provide further evidence for cold mantle atop the slab. These interpretations are consistent with a ~40 km-thick cold viscous TBL atop the slab (*4*, *20*, *59*) (Figure 6). Numerical models predict a TBL (Figure S13) with a high shear viscosity that causes it to be dragged down with the subducting plate, facilitating the down-dip and transport of expelled slab fluids towards the back-arc (*7*). Such down-dip fluid transport thus reconciles the observed horizontal and vertical offset between high Q_S^{-1} and high V_P/V_S (Figure 6).

The highest Q_S^{-1} lies in the back-arc of Dominica and correlates with low V_S (~4.3 km/s) but only moderately elevated V_P/V_S (1.75-1.80) (*43*, *45*) (Figures 4, 7b). To understand whether

such high Q_S^{-1} can be explained by temperature alone, we use 2-D kinematic geodynamic models to predict the thermal structure beneath the LAA (*45*). We then predict Q_S^{-1}, assuming the wedge is dry and melt-free (*52*). To account for our imaging capability, we calculate synthetic t^* values through these models, then invert these synthetic data for Q_S^{-1} as with our actual data. Our models (Figure S13) predict a maximum mantle wedge temperature of (~1350°C) that yields a maximum $1000/Q_S$ = 7-9, which is much weaker than observed ($1000/Q_S$ = 17-25). Therefore, temperature alone cannot explain such high mantle attenuation.

The overlap between high Q_S^{-1} and low V_S, along with negligible Q_κ^{-1} in the core of the mantle wedge, means that the observed anomalies likely result primarily from intrinsic rather than scattering attenuation (*27*, *34*). Moreover, seismograms from OBS stations in the back-arc show simple, low-frequency *S*-waves with minimal coda (Figure S5). Therefore, assuming negligible scattering attenuation in the mantle wedge, we further investigate its properties by forward modelling Q_S^{-1} and V_S using the *Very Broadband Rheology calculator* (*53*). High Q_S^{-1} in the mantle wedge cannot be explained solely by fluids because increasing intrinsic attenuation tradeoffs with grain growth that, in turn, reduces attenuation (*25*). We compute the likely melt fraction - temperature field using an ensemble weight of the joint probability distribution for two anelastic methods: the Andrade-pseudoperiod and modified Burgers models (*52*). We use the depth range of 70-105 km to compute averaged representative seismic properties, accounting for standard errors ($1000/Q_S$ = 16; V_S = 4.3 km/s) in the back-arc of Dominica. Both anelastic models yield similar temperature and melt fraction distributions, and the overall ensemble result is shown in Figure S14. There is a clear tradeoff between increasing temperatures and decreasing melt fractions. Still, if we take a maximum mantle wedge temperature of 1350°C from our geodynamic predictions (Figure S13), the most likely melt fraction in the mantle wedge is 1.5-2.0%.

Independent evidence for extensive melt comes from volcanological and geochemical constraints. Of all islands of the LAA, Dominica, with five active volcanic centres (Figure 1), has the highest erupted volume of magma over the last 100 kyr (*60*) (Figure 7). Moreover, Dominica-Guadeloupe is where an along-arc peak in $\delta^{11}B$ values of melt inclusions indicates significant fluxing of volatiles from serpentinised slab mantle (*19*) (Figure 7). Our Q^{-1} images show that these fluids contribute most strongly to flux melting of the back-arc mantle.

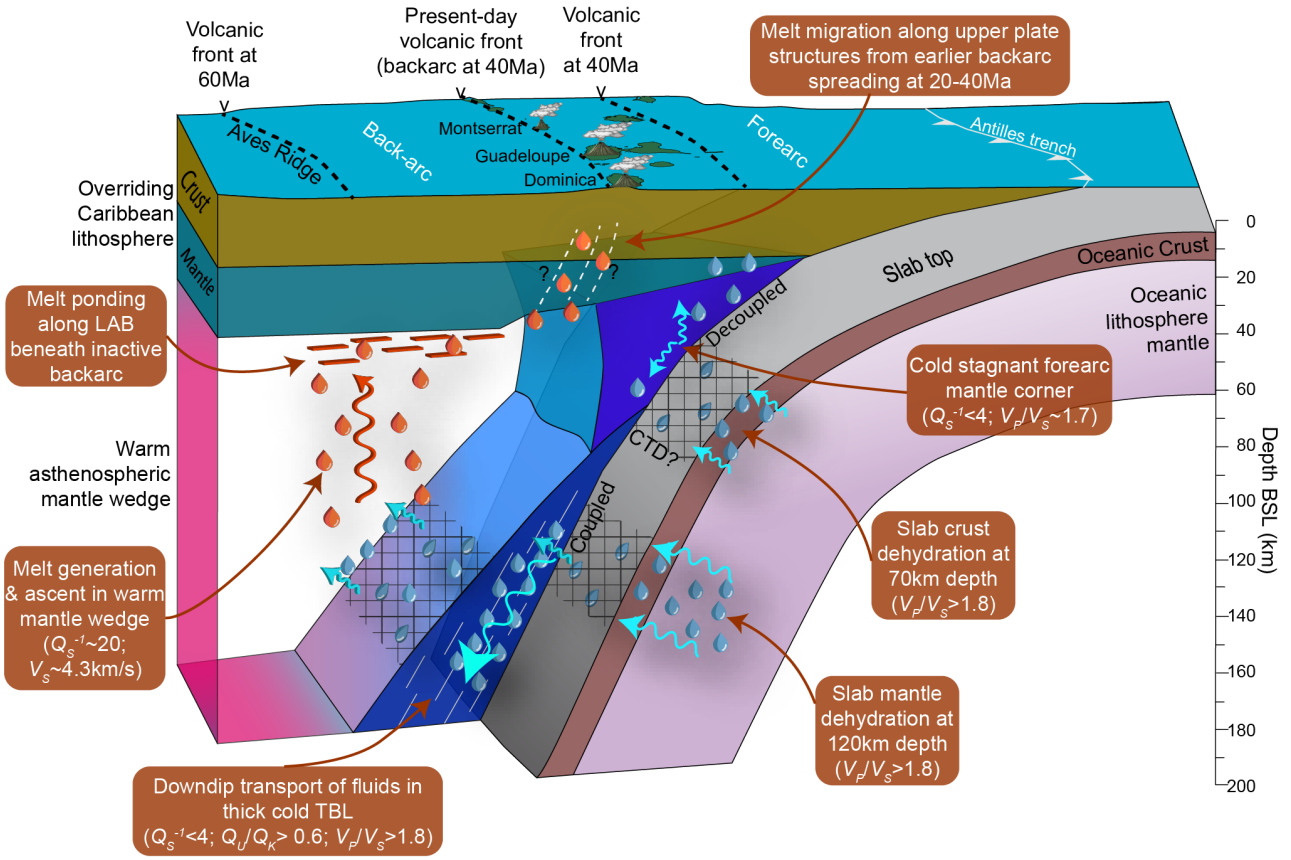

Figure 6: Schematic view of dehydration and melting processes in the mantle wedge beneath the LAA based on combined interpretation of seismic attenuation and velocities. The 3-D perspective view is cut away in two locations to show the top of the slab and the top of the TBL. Blue drip symbols and arrows indicate interpreted volatiles and their pathways; red shows melt. The areas with hatching indicate 'wet' surfaces. Previous arc positions are from Allen et al. (*40*). 2x vertical exaggeration. LAB = lithosphere-asthenosphere boundary; TBL = thermal boundary layer; CTD = coupling transition depth.

The highest Q^{-1} in the back-arc mantle wedge ($1000/Q_S$ = 17-25) is similar to that observed in Pacific-type subduction zones where the downgoing lithosphere is consumed at a faster rate, such as Nicaragua (*29*), Marianas (*27*), New Zealand (*26*), and Tonga-Lau (*28*). In most of these subduction zones, there is typically a broad zone of high attenuation ($1000/Q_P$ > 10; $1000/Q_S$ > 12) that lies in the mantle wedge directly beneath the volcanic front (*29*, *33*, *34*, *61*, *62*). The exception to this pattern is Tonga-Lau, where sub-arc attenuation is low, and back-arc attenuation is high, likely related to active back-arc spreading and decompression melting (*28*). Thus, our LAA result, where the attenuating wedge core is offset by 40-70 km into the back-arc (Figure 2), is more similar to Tonga-Lau. Reasonably slow V_S (<4.3 km/s) extending some 200 km into the LAA back-arc (*45*) provides further evidence that the back-arc mantle wedge is hotter and contains a higher melt fraction than the sub-arc mantle. Our result is counterintuitive in that, in contrast to the Lau Basin, there is no evidence of active spreading in the Grenada Basin behind the LAA (*40*). A key implication of this result is

that the volatiles driving flux melting derive mainly from the deeper pulse of slab mantle dehydration at 120-140 km depth and that melt eventually reaches the active volcanic arc by an indirect, non-vertical pathway (Figure 6). With high Q^{-1} and low V_S (*43*, *45*) extending up to the base of the overriding Caribbean plate, in the back-arc and offset from the active arc (Figure 9c), along with a corresponding substantial negative velocity gradient at the base of the lithosphere below the back-arc (*47*), we favour a model of ponding of partial melt along the LAB (*63*) beneath the back-arc (Figure 6).

The highest Q_S^{-1} anomaly near Dominica does not spatially coincide with any projected positions of subducted FZs, with the Marathon and Mercurius FZs projected ~100 km to the NNW (Figures 4 and 6d). In the along-arc direction (Figure 3, Section E-E'), the highest Q_S^{-1} in the mantle wedge lies atop low Q_S^{-1}, high Q_κ^{-1}/Q_μ^{-1}, and high V_P/V_S in the TBL, suggesting a direct link between mantle wedge melting and pre-existing slab hydration. We attribute the offset of the FZs, and their clear hydration imprint (*19*, *43*), with wedge anomalies, to the migration of melt from the back-arc towards the arc, the opposite direction to plate convergence.

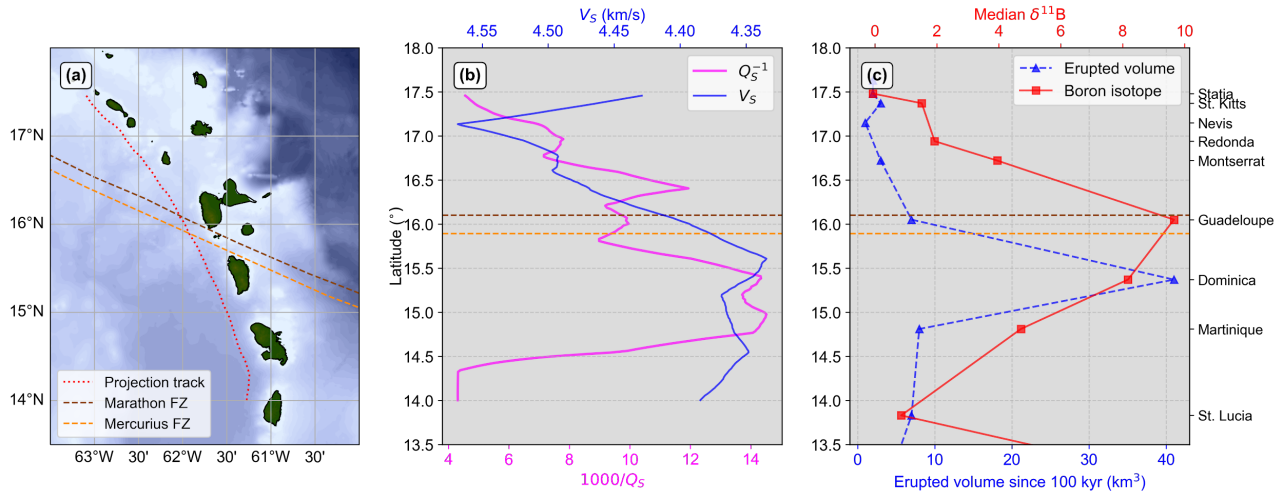

Figure 7: Comparing seismic properties with magmatism along the LAA. (a) Map showing the line along which seismic properties are plotted (red dotted line) and projected fracture zone (FZ) positions. b) Along-arc Q_S^{-1} variation at 95 km depth from this study and V_S at 95 km depth (*45*). Note that the V_S axis has been reversed. c) Along-arc variability in total erupted volume (dashed blue line and points) (*60*) and boron isotope composition of melt inclusions from erupted volcanic rocks (red line and points) (*19*). The horizontal dashed lines in (b) and (c) show the intersection of subducted fracture zones with the back-arc profile (*19*).

3.3 Implications for arc volcanism

Our result is consistent with a model that explains volatile pathways and melting from slab to arc (Figure 6). Expelled volatiles from the slab crust dehydration do not likely enter the warm

asthenospheric wedge and thus do not contribute to flux melting in the mantle due to the large cold forearc corner. However, we cannot exclude whether the TBL transports some of these crustal-derived fluids down-dip (*7*). Volatiles from the second deeper pulse of slab dehydration are carried further down-dip in the cool, viscous TBL atop the slab. These fluids are eventually released into the back-arc mantle, resulting in the generation of melt which is transported to the LAB of the overriding plate beneath the back-arc. The lack of active back-arc spreading (*40*), along with a strong negative S-to-P receiver function phase at 60 km depth beneath the back-arc, and slow V_s (<4.4 km/s) anomaly (*43*, *45*) indicate melt ponding at the base of the mostly cool upper plate (*45*, *47*) (Figure 6).

Previously, mechanisms of melt ponding beneath the upper plate in a subduction zone setting have been associated with gaps in arc volcanism (*23*). However, the seismic attenuation and velocity structure (*43*, *45*, *47*) imply that the strongest melt generation and subsequent ponding is in the back-arc of the Dominica segment, the most magmatically productive island of the entire LAA (Figure 7). Given that accumulated melt at the LAB must reach the active volcanoes, an outstanding question is: what controls the localisation of the frontal arc? We suggest that past tectonic history is a key factor here: the LAA migrated trenchward at 40 Ma from the Aves Ridge to the Limestone Caribees, followed by a forward step to its present-day position at 20 Ma, which was the previous back-arc spreading axis at 20-40 Ma (Figure 6). Back-arc spreading accompanied arc volcanism at these two earlier arcs (*40*). Thus the forward jump at 20 Ma built the present-day volcanic front at the preceding back-arc spreading centre (Figure 6). The resulting inherited permeability structure is what we believe helps to channel and focus melt from the back-arc, following inclined decompaction channels along the LAB (*8*) and migrating toward a pinch zone with thinner sub-arc lithosphere (*7*, *8*, *22*, *23*). Receiver functions verify this model by highlighting abnormally thin sub-arc lithosphere (40 km) beneath Dominica (*48*). Melt migration is further facilitated by arc-normal tension (*11*), consistent with tectonic structures of the LAA (*64*). Melt channels through the upper plate are likely very narrow (e.g., ~15 km width) (*1*, *10*) and not imagable with our methodology. A further question remains over why there is a barrier to melts ascending vertically through the upper plate into the back-arc. Permeability may be reduced by the low temperature of the upper plate beneath the back-arc, as supported by seismic velocities (*45*), promoting crystallisation (*23*). Overall, our model uniquely involves simultaneous ponding and volcanism (Figure 6), previously thought to

individually represent end-member steady-state subduction and slab advance configurations (*23*).

Therefore, the classic paradigm in which volatiles and associated melt generated travels vertically from slab to sub-arc crustal magma chambers is not universally true. Instead, we have shown that even though volatiles can be released from the sub-arc slab, fluid and trajectory can be more circuitous, with arc magma being sourced from the back-arc mantle wedge. Geodynamic models that include compaction predict a similar trajectory of volatiles and melt (*7*, *8*). The critical factors that make this melt trajectory particularly apparent in the LAA are (i) subduction of old lithosphere, which causes deep dehydration of the slab mantle, and (ii) a slow convergence rate that generates a thick viscous TBL, which has a heterogeneous hydration state preconditioned by laterally variable slab water content, and (iii) historical migration of the arc and upper plate which preconditions its permeability structure. However, down-dip fluid migration in the TBL may be prevalent regardless of slab age and may transport fluids down-dip for younger slabs where slab devolatilisation occurs at shallower depths (*7*). Moreover, arc migration is common in many subduction zones (*24*). Therefore, our observations for the LAA represent an end-member case that makes lateral fluid and melt pathways more apparent, but there may be more subtle evidence of these processes in other subduction zones. Such subtle effects might be apparent in published Q^{-1} tomography results, but a reevaluation might be required in light of our results for the LAA.

Overall, our result for the LAA demonstrates how feedback between processes across the entire subduction system, such as slab dehydration, melt pathways in the mantle, and tectonic evolution of both the subducting and upper plates governs arc magmatism. Our model, and melt ponding in particular, has implications for arc productivity, whether melt supply to the arc is steady-state or episodic, and how the LAA will further evolve in the future.

4 Conclusions

We have studied the seismic attenuation structure of a global end-member subduction zone in the Eastern Caribbean and integrated our results with previously determined seismic velocities. A large, weakly attenuating, and hence cold, mantle corner beneath the fore-arc and arc prevents melts from ascending along a vertical path. High bulk-to-shear attenuation and high V_P/V_S in a 40 km-thick layer above the slab reflect a cold TBL that facilitates downdip transport of fluids at the base of the mantle wedge. Fluids transported by the TBL before being released into the warm convecting wedge would affect estimates of slab surface temperatures from geochemical markers. Once removed from the TBL, the fluids ascend into the hot mantle wedge beneath the back-arc, where substantial melt fractions (1-2%) explain high Q_S^{-1} ($1000/Q_S$ = 17-25). Interpreting attenuation in the context of the past tectonic history in the Eastern Caribbean highlights feedback between slab dehydration processes, mantle wedge melt transport, and the tectonic evolution of the subduction system. We infer that melt accumulates at the base of the overriding plate below the back-arc. Some of this melt reaches the arc via an inclined pathway along the LAB. It then percolates through the upper plate via extensional structures formed during active back-arc spreading before the arc jumped forward to its current position at 20 Ma. Fluid transport towards the back-arc in the cold TBL explains why substantial mantle wedge attenuation is spatially offset from enhanced plate hydration along subducting FZs and associated domain boundary. Our study allows us to differentiate free fluids from melt in the mantle wedge, highlighting a sub-vertical pathway conditioned by a combination of mantle wedge conditions and structures inherited from the tectonic history of the arc. These signatures are made more evident by the slow subduction of old, tectonised lithosphere beneath the LAA, enhancing deep dehydration and with a thicker TBL than Pacific-type subduction zones. Even if not as easy to image, similar feedback processes will likely govern melt supply to the volcanic arc in other subduction zones.

Materials and Methods

Seismic data collection and preprocessing.

Our data come from the *VoiLA* (Volatiles in the Lesser Antilles) experiment, which included an ocean-bottom seismometer (OBS) deployment from March 2016 to May 2017 (*38*, *49*) (cruises JC133; JC149). The 34-station OBS network (Figure 1) significantly extends the coverage of existing permanent seismic networks on the islands, improving the resolution capability in the fore- and back-arc. We included stations from existing land networks in our study, with the corresponding FDSN network codes as follows: CU (*65*), G (*66*), GL, MQ, NA (*67*) TR, and WI (*68*).

Our local earthquake catalogue (Figure 1) (*38*) includes arrival times, local magnitudes and relocations inside a region-specific 1-D velocity model from the VoiLA OBS network and existing land stations. To eliminate possible complexities in ray-path propagation effects for shallow paths (*27*, *69*) and poorly constrained events with shallow depths, we only used events with a hypocentral depth of greater than 15 km. We excluded events with poor location constraints, filtering with a maximum azimuthal gap of 220°. Our starting catalogue has 296 events with these criteria, ranging from M_L 2.0 to 6.6.

Before the t^* inversion, we corrected the seismograms for instrument response, converted them to displacement, and rotated the horizontal components into a radial-transverse coordinate system.

Inversion for t^*

We inverted amplitude spectra of *P*- and *S*-waves for the path-averaged attenuation operator, t^*. We followed a similar strategy to Wei and Wiens (*28*), which follows the broad inversion approach taken in several previous attenuation tomography studies in subduction zones (*27–30*, *69*).

We inverted amplitude spectra of *P*- and *S*-waves for each event-station pair for the attenuation operator, $t^*_{.}$ For the k^{th} earthquake recorded at the j^{th} station, the displacement spectrum is defined as:

$$A_{jk}(f_i) = \frac{C_{jk} M_{ok} e^{-\pi f_i^{1-\alpha} t^*_{0jk}}}{1+\left(\frac{f_i}{f_{ck}}\right)^2} \quad \text{Eq. 1}$$

where C_{jk} is a constant factor for each observation accounting for geometric spreading, the free surface effect and source radiation (*70*); M_{ok} and f_{ck} are the seismic moment and corner frequency, respectively; t^*_{0jk} is the attenuation factor at 1 Hz; and α expresses the frequency dependence of attenuation (*71*). We used a 1-D velocity model for the LAA (*38*) for computing the C_{jk} corrections. We used a non-negative least-squares inversion to solve for t^*_{0jk}, and M_{ok} and f_{ck} for each event.

For each earthquake, we first computed the best-fitting corner frequency and moment using a grid-search within a range of prescribed stress drops, $\Delta\sigma$, varying from 0.1 to 100 MPa (*27*), which is within typical observed $\Delta\sigma$ values (*38*), assuming circular rupture and a given empirical relationship between M_L and M_w:

$$f_c = 0.49\beta\left(\frac{\Delta\sigma}{M_0}\right)^{\frac{1}{3}} \quad \text{Eq. 2}$$

where β is the *S*-wave velocity, which we assume to be 4.0 km/s (*38*). We computed M_0 from a regression between M_L and M_w calculated from waveform moment tensor inversion of the VoiLA dataset (*72*):

$$M_w = 1.05\, M_L - 0.42 \quad \text{Eq. 3}$$

The resulting spectral-derived Moment Magnitudes (M_w) from *P*- and *S*-waves are consistent with each other and are similar to corresponding Local Magnitudes (*38*) (Figure S1) showing that our inversions recover reasonable source parameters.

We selected appropriate window lengths for computing spectra. We found that 3 s long windows, starting 0.5 s and 1.0 s before the manually picked arrival for *P*- and *S*-waves, respectively, produced the greatest number of good-fitting t^* observations (Figure S2). Longer windows introduced a bias due to secondary phases. We computed signal and noise spectra using a multi-taper approach (*73*). A t^* measurement was acceptable if it had a spectral misfit of <20%. We also excluded observations with small t^* values that led to unrealistic t^* path-averaged values (<0.0007). Figure S5 shows an example of the t^* fitting process for an example event at 182 km and recorded at stations situated in the back-arc,

arc, and fore-arc. We used the vertical component for *P*-waves and found the widest bandwidth where the signal-to-noise ratio exceeds 2.0, with a minimum frequency bandwidth of 2 Hz, to determine the frequency range used for the t^* inversion. We used the transverse component for *S*-waves, ensuring a minimum signal-to-noise ratio of 1.8 and a minimum frequency bandwidth of 1.2 Hz. The transverse component minimises the effect of potential *P*-to-*S* conversions (*30*). We excluded frequencies under 0.5 Hz for P- and S-waves to avoid ocean swell noise.

Inversion for t^* requires assumptions about the remaining parameters of Eq. 1, f_c and α. We experimented with different assumptions about f_c. First, we required that the best-fitting f_c lies within the frequency band of spectral fitting (Figure 2b). This approach avoids unrealistic values of corner frequency in the t^* inversion due to inherent tradeoffs between the f_c source term and the t^* path term. At least four high-quality spectral observations were required to determine f_c for an event. Although f_c and M_o can be computed separately for *P*-and *S*-waves, the latter on OBS records are often band-limited, resulting in a poorly constrained f_c, which results in fewer *S*-wave t^* observations. Alternatively, we could require that f_c for *S*-waves is equal to that of *P*-waves (*28*) or that they differ by a scaling factor of 1.5, as theoretically expected for circular ruptures (*27*, *74*). We chose the assumptions for our dataset that produced the greatest number of good-fitting t^* measurements. Our resulting preference was to assume $f_{c(S)} = f_{c(P)}$ (*28*). Even with this assumption, moment magnitudes from *S*-wave spectra closely follow those from *P*-waves (Figure S1). We also experimented with varying the frequency-dependent term, α. We found that when α exceeds 0.6, the computed M_w deviated from M_L, yielding unrealistic magnitudes. We found a weakly constrained minimum in *P*-wave spectral misfits at $\alpha = 0.30$ if we included the deepest events in the dataset (>175 km depth), which will have the longest paths through the mantle wedge. We used $\alpha = 0.27$ since it is consistent with experimental results relevant to the mantle wedge (*52*, *54*, *75*), so our results can be directly compared with published attenuation studies of other subduction zones (*27*, *29*, *30*, *33*). Although frequency dependence affects individual t^* values, it is unlikely to affect overall Q^{-1} patterns in the final tomographic images (*76*).

Since the main aim of our study is to analyse mantle structure in the LAA, we considered possible frequency-dependent site effects from shallow crustal geological heterogeneity. Instead of inverting for a constant t^* station term in the tomographic inversion, we estimated residual spectra (*30*, *69*). We stacked and smoothed residual spectra for each station and

computed the resulting median spectrum as the site effect. Site spectra (Figures S3 & S4) show no systematic site effects reflecting the local geology and the station's position in the subduction zone (i.e. back-arc versus arc versus fore-arc). We then repeated the t^* inversion process after removing the site effects from the original spectrum. Removal of the site effects reduced spectral misfit by correcting for spectral peaks and holes. This process allowed 14% and 40% more *P*- and *S*-wave t^* observations, respectively, to be used. The final Q^{-1} inversions do not substantially change when removing the site effects (Figure S11).

With our optimum assumptions described above, we have a database of 2,245 and 1,557 good-fitting t^* observations from 135 events for *P*-waves and *S*-waves, respectively (Table 1). For weakly-attenuating paths, we typically fit *P*-wave spectra up to 20 Hz on OBS stations; strongly attenuating raypaths limit *S*-wave bandwidths to <4 Hz (Figure S5). Comparing t^* for *P*- and *S*-waves for the same event-station paths indicates an overall Q_P/Q_S ratio of ~1.5. We did not find any obvious spatial pattern in path-averaged Q_P/Q_S.

Attenuation imaging method

We restrict the areal extent of tomographic imaging by only including events and stations within the region of dense raypath coverage along the linear arc segment from St. Kitts in the north to Saint Lucia in the south (Figure 1). This refined area leaves a dataset of 122 events, with 1,499 *P*-wave observations and 1,039 *S*-wave observations. We inverted t^* measurements for Q^{-1} images using iterative damped least-squares (*77*) and raytracing based on a 3-D seismic velocity model for the LAA developed using travel-times from the same dataset (*43*). We weight each t^* observation relative to the computed spectral misfit. We determined the damping parameter for each inversion by evaluating trade-off curves between data and model parameter variance. For the tomographic inversions, the homogeneous Q^{-1} starting model came from the path-averaged t^* for *P*- and *S*-waves individually ($1000/Q_P$=1.6; $1000/Q_S$=4.3). We also jointly inverted for bulk and shear moduli attenuation (Q_κ, Q_μ, respectively) using *P*- and *S*-wave t^* data for the same source-receiver pair to compute a Q_κ^{-1}/Q_μ^{-1} ratio (*30*). We used 505 *P*- and *S*-wave observation pairs for this joint inversion.

Our first aim was to determine the arc-perpendicular structure of the subduction zone before looking into possible along-arc variations. Therefore, we generated a 2-D inversion grid aligned perpendicular to the arc and trench. The grid was identical to that used by Bie et

al. (*43*) to perform velocity tomography from the same earthquake observations. The spatial variation of ray-path derivative weight sum (DWS) guided the grid design. In the horizontal direction. There is a minimum grid spacing of 25 km in the model's centre, beneath the inner fore-arc, arc and eastern back-arc, where the highest ray density is. There is a vertical spacing of 10 km between 0 and 30 km depth in the upper plate crust, increasing to 20 km between 45 and 65 km depth, and a 30 km depth spacing between 65 and 200 km depth in the mantle wedge region (Figure S6). For the 3-D tomographic imaging, we use a grid spacing of 25 km in the arc-parallel direction. Compared to the 2-D inversion, the 3-D model reduces overall data variance for the same t^* dataset by 30% and 19% for *P*- and *S*-waves.

Assessment of model resolution

We assessed model resolution based on several analyses (*78*) (Figure S6). We evaluated the diagonal element of the model resolution matrix, the spread function and the 70% contour of each row of the resolution matrix. The results are shown for the 2-D inversion in Figure S6a and the 3-D inversion in Figures S7-S8, respectively. For the Q_κ^{-1}/Q_μ^{-1} image, we took the resolution limit from the 3-D Q_S inversion. We also carried out recovery tests using checkerboards in which we designed anomaly patterns based on our inversion grid (whose spacing is non-uniform) with two grid configurations. (1) a coarse (2x2 grid spacing; i.e., a minimum 50x50 km anomalies in the centre of the model) (Figure 4b-i), and (2) fine (1x1 grid spacing; i.e., a minimum 25x25 grid spacing in the centre of the model) (Figure 4b-ii). We based checkerboard amplitudes on the low Q^{-1} from the tomographic starting model and a high Q^{-1} of 1000/Q=50. The results for the checkerboard tests with the 3-D inversion are shown in Figures S9 and S10.

These tests show that we can resolve the top of the down-going plate from ~140 km inboard of the trench to ~160 km depth due to the maximum observed seismicity in this region. Most smearing occurs in the vertical direction or towards the back-arc at shallower depths. We can image the supra-slab area in the back-arc to 130 km west of the arc and in the fore-arc to ~100 km east of the arc. Resolution peaks in the mantle wedge region between 40 and 140 km depth, where the spread function is low (<2), and smearing contours indicate minimal smearing in the vertical direction (Figure S6a). For the 2-D inversion, we consistently resolve the structure of the 50x50 km anomalies in the mantle wedge and fore-arc and recover their *Q* amplitudes to within ~8% of the input in the mantle wedge region (Figure S6b-i). We are

also able to resolve the alternating patterns of 25x25 km anomalies, although resolution diminishes in the back-arc and at shallow depths (<20 km) (Figure S6-ii). The amplitudes of the high Q^{-1} anomalies are also muted (~20% recovery in the mantle wedge region) with the finer scale checker-pattern anomalies. For the 3-D inversion (Figures S7 and S8), we cannot resolve the upper plate at crustal depths beneath Dominica due to the lack of broadband stations on the island. In contrast, at mantle wedge depths, the resolution is strongest in the Dominica region due to the high rate of intermediate-depth seismicity in this region of the LAA. There is more smearing in the Montserrat-Guadeloupe region due to the lack of deep seismicity. The 3-D checkerboard tests (Figures S9 and S10) show diminished resolution, and we cannot consistently resolve anomalies with dimensions of <50 km.

Testing assumptions of the t* inversion on the tomographic results

We have assumed that $f_{c(S)} = f_{c(P)}$, although other studies use $f_{c(S)} = f_{c(P)} / 1.5$ (*27*, *74*). We have also removed site spectra before taking t^* measurements. It is worth considering whether these assumptions introduce potential biases into our tomographic inversions. Therefore, we carried out two additional 2-D inversions of Q_S^{-1}, accounting for each of these assumptions individually. The results are shown in Figure S11. These inversions are consistent with the main anomaly shapes and amplitudes as per our main inversion result.

References

1. P. C. England, R. F. Katz, Melting above the anhydrous solidus controls the location of volcanic arcs. *Nature*. **467**, 700–703 (2010).
2. T. L. Grove, C. B. Till, M. J. Krawczynski, The role of H2O in subduction zone magmatism. *Annu. Rev. Earth Planet. Sci.* **40**, 413–439 (2012).
3. M. W. Schmidt, S. Poli, Experimentally based water budgets for dehydrating slabs and consequences for arc magma generation. *Earth Planet. Sci. Lett.* **163**, 361–379 (1998).
4. R. J. Stern, Subduction Zones. *Rev. Geophys.* **40**, 3-1-3–38 (2002).
5. E. M. Syracuse, P. E. van Keken, G. A. Abers, The global range of subduction zone thermal models. *Phys. Earth Planet. Inter.* **183**, 73–90 (2010).
6. I. Wada, K. Wang, Common depth of slab-mantle decoupling: Reconciling diversity and uniformity of subduction zones. *Geochem. Geophys. Geosystems*. **10** (2009), doi:10.1029/2009GC002570.
7. N. G. Cerpa, I. Wada, C. R. Wilson, Fluid migration in the mantle wedge: Influence of mineral grain size and mantle compaction. *J. Geophys. Res. Solid Earth*. **122**, 6247–6268 (2017).
8. C. R. Wilson, M. Spiegelman, P. E. van Keken, B. R. Hacker, Fluid flow in subduction zones: The role of solid rheology and compaction pressure. *Earth Planet. Sci. Lett.* **401**, 261–274 (2014).
9. C. B. Till, A. J. R. Kent, G. A. Abers, H. A. Janiszewski, J. B. Gaherty, B. W. Pitcher, The causes of spatiotemporal variations in erupted fluxes and compositions along a volcanic arc. *Nat. Commun.* **10**, 1350 (2019).
10. A. Perrin, S. Goes, J. Prytulak, D. R. Davies, C. Wilson, S. Kramer, Reconciling mantle wedge thermal structure with arc lava thermobarometric determinations in oceanic subduction zones. *Geochem. Geophys. Geosystems*. **17**, 4105–4127 (2016).
11. H. Andikagumi, C. G. Macpherson, K. J. W. McCaffrey, *J. Geophys. Res. Solid Earth*, in press, doi:10.1029/2019JB017391.
12. G. A. Abers, P. E. van Keken, C. R. Wilson, Deep decoupling in subduction zones: Observations and temperature limits. *Geosphere*. **16**, 1408–1424 (2020).
13. E. M. Syracuse, G. A. Abers, Global compilation of variations in slab depth beneath arc volcanoes and implications. *Geochem. Geophys. Geosystems*. **7** (2006), doi:10.1029/2005GC001045.
14. B. C. Kerswell, M. J. Kohn, T. V. Gerya, *Geochem. Geophys. Geosystems*, in press, doi:10.1029/2020GC009304.
15. N. Harmon, D. K. Blackman, Effects of plate boundary geometry and kinematics on mantle melting beneath the back-arc spreading centers along the Lau Basin. *Earth Planet. Sci. Lett.* **298**, 334–346 (2010).
16. H. Iwamori, Transportation of H2O and melting in subduction zones. *Earth Planet. Sci. Lett.* **160**, 65–80 (1998).
17. J. H. Davies, D. J. Stevenson, Physical model of source region of subduction zone volcanics. *J. Geophys. Res. Solid Earth*. **97**, 2037–2070 (1992).
18. L. B. Cooper, D. M. Ruscitto, T. Plank, P. J. Wallace, E. M. Syracuse, C. E. Manning, Global variations in H2O/Ce: 1. Slab surface temperatures beneath volcanic arcs. *Geochem. Geophys. Geosystems*. **13** (2012), doi:10.1029/2011GC003902.
19. G. F. Cooper, C. G. Macpherson, J. D. Blundy, B. Maunder, R. W. Allen, S. Goes, J. S. Collier, L. Bie, N. Harmon, S. P. Hicks, A. A. Iveson, J. Prytulak, A. Rietbrock, C. A. Rychert, J. P. Davidson, Variable water input controls evolution of the Lesser Antilles volcanic arc. *Nature*. **582**, 525–529 (2020).

20. C. Kincaid, I. S. Sacks, Thermal and dynamical evolution of the upper mantle in subduction zones. *J. Geophys. Res. Solid Earth*. **102**, 12295–12315 (1997).
21. G. Ha, L. G. J. Montési, W. Zhu, *Geochem. Geophys. Geosystems*, in press, doi:10.1029/2020GC009253.
22. A.-M. Cagnioncle, E. M. Parmentier, L. T. Elkins-Tanton, Effect of solid flow above a subducting slab on water distribution and melting at convergent plate boundaries. *J. Geophys. Res. Solid Earth*. **112** (2007), doi:10.1029/2007JB004934.
23. S. Rondenay, L. G. J. Montési, G. A. Abers, New geophysical insight into the origin of the Denali volcanic gap. *Geophys. J. Int.* **182**, 613–630 (2010).
24. B. R. Jicha, S. M. Kay, Quantifying arc migration and the role of forearc subduction erosion in the central Aleutians. *J. Volcanol. Geotherm. Res.* **360**, 84–99 (2018).
25. G. A. Abers, K. M. Fischer, G. Hirth, D. A. Wiens, T. Plank, B. K. Holtzman, C. McCarthy, E. Gazel, Reconciling mantle attenuation-temperature relationships from seismology, petrology, and laboratory measurements. *Geochem. Geophys. Geosystems.* **15**, 3521–3542 (2014).
26. D. Eberhart-Phillips, S. Bannister, M. Reyners, Attenuation in the mantle wedge beneath super-volcanoes of the Taupo Volcanic Zone, New Zealand. *Geophys. J. Int.* **220**, 703–723 (2020).
27. S. H. Pozgay, D. A. Wiens, J. A. Conder, H. Shiobara, H. Sugioka, Seismic attenuation tomography of the Mariana subduction system: Implications for thermal structure, volatile distribution, and slow spreading dynamics. *Geochem. Geophys. Geosystems.* **10** (2009), doi:10.1029/2008GC002313.
28. S. S. Wei, D. A. Wiens, *J. Geophys. Res. Solid Earth*, in press.
29. C. A. Rychert, K. M. Fischer, G. A. Abers, T. Plank, E. Syracuse, J. M. Protti, V. Gonzalez, W. Strauch, Strong along-arc variations in attenuation in the mantle wedge beneath Costa Rica and Nicaragua. *Geochem. Geophys. Geosystems.* **9** (2008).
30. J. C. Stachnik, G. A. Abers, D. H. Christensen, Seismic attenuation and mantle wedge temperatures in the Alaska subduction zone. *J. Geophys. Res. Solid Earth*. **109** (2004).
31. B. Budiansky, E. E. Sumner Jr., R. J. O'Connell, Bulk thermoelastic attenuation of composite materials. *J. Geophys. Res. Solid Earth*. **88**, 10343–10348 (1983).
32. X. Liu, D. Zhao, S. Li, Seismic attenuation tomography of the Northeast Japan arc: Insight into the 2011 Tohoku earthquake (Mw 9.0) and subduction dynamics. *J. Geophys. Res. Solid Earth*. **119**, 1094–1118 (2014).
33. J. Nakajima, S. Hada, E. Hayami, N. Uchida, A. Hasegawa, S. Yoshioka, T. Matsuzawa, N. Umino, Seismic attenuation beneath northeastern Japan: Constraints on mantle dynamics and arc magmatism. *J. Geophys. Res. Solid Earth*. **118**, 5838–5855 (2013).
34. B. Schurr, G. Asch, A. Rietbrock, R. Trumbull, C. Haberland, Complex patterns of fluid and melt transport in the central Andean subduction zone revealed by attenuation tomography. *Earth Planet. Sci. Lett.* **215**, 105–119 (2003).
35. E. M. Syracuse, G. A. Abers, K. Fischer, L. MacKenzie, C. Rychert, M. Protti, V. González, W. Strauch, Seismic tomography and earthquake locations in the Nicaraguan and Costa Rican upper mantle. *Geochem. Geophys. Geosystems*. **9** (2008), doi:https://doi.org/10.1029/2008GC001963.
36. M. Reyners, D. Eberhart-Phillips, G. Stuart, Y. Nishimura, Imaging subduction from the trench to 300 km depth beneath the central North Island, New Zealand, with Vp and Vp/Vs. *Geophys. J. Int.* **165**, 565–583 (2006).
37. J. A. Conder, D. A. Wiens, Seismic structure beneath the Tonga arc and Lau back-arc basin determined from joint Vp, Vp/Vs tomography. *Geochem. Geophys. Geosystems*. **7** (2006), doi:10.1029/2005GC001113.

38. L. Bie, A. Rietbrock, S. Hicks, R. Allen, J. Blundy, V. Clouard, J. Collier, J. Davidson, T. Garth, S. Goes, N. Harmon, T. Henstock, J. van Hunen, M. Kendall, F. Krüger, L. Lynch, C. Macpherson, R. Robertson, K. Rychert, S. Tait, J. Wilkinson, M. Wilson, Along-Arc Heterogeneity in Local Seismicity across the Lesser Antilles Subduction Zone from a Dense Ocean-Bottom Seismometer Network. *Seismol. Res. Lett.* **91**, 237–247 (2020).
39. D. Schlaphorst, J.-M. Kendall, B. Baptie, J. L. Latchman, S. Tait, Gaps, tears and seismic anisotropy around the subducting slabs of the Antilles. *Tectonophysics.* **698**, 65–78 (2017).
40. R. W. Allen, J. S. Collier, A. G. Stewart, T. Henstock, S. Goes, A. Rietbrock, The role of arc migration in the development of the Lesser Antilles: A new tectonic model for the Cenozoic evolution of the eastern Caribbean. *Geology*. **47**, 891–895 (2019).
41. R. G. Davy, J. S. Collier, T. J. Henstock, T. V. Consortium, *J. Geophys. Res. Solid Earth*, in press, doi:10.1029/2019JB019100.
42. D. Schlaphorst, J.-M. Kendall, J. S. Collier, J. P. Verdon, J. Blundy, B. Baptie, J. L. Latchman, F. Massin, M.-P. Bouin, Water, oceanic fracture zones and the lubrication of subducting plate boundaries—insights from seismicity. *Geophys. J. Int.* **204**, 1405–1420 (2016).
43. L. Bie, S. Hicks, A. Rietbrock, S. Goes, J. Collier, C. Rychert, N. Harmon, B. Maunder, Imaging slab-transported fluids and their deep dehydration from seismic velocity tomography in the Lesser Antilles subduction zone. *Earth Planet. Sci. Lett.* **586**, 117535 (2022).
44. B. Braszus, S. Goes, R. Allen, A. Rietbrock, J. Collier, N. Harmon, T. Henstock, S. Hicks, C. A. Rychert, B. Maunder, J. van Hunen, L. Bie, J. Blundy, G. F. Cooper, R. Davy, J. M. Kendall, C. Macpherson, J. Wilkinson, M. Wilson, Subduction history of the Caribbean from upper-mantle seismic imaging and plate reconstruction. *Nat. Commun.* **12**, 4211 (2021).
45. N. Harmon, C. A. Rychert, S. Goes, B. Maunder, J. Collier, T. Henstock, L. Lynch, A. Rietbrock, the V. W. Group, *Geochem. Geophys. Geosystems*, in press, doi:10.1029/2021GC009707.
46. D. Schlaphorst, N. Harmon, J. M. Kendall, C. A. Rychert, J. Collier, A. Rietbrock, S. Goes, the V. Team, *Geochem. Geophys. Geosystems*, in press, doi:10.1029/2021GC009800.
47. B. Chichester, C. Rychert, N. Harmon, J. Collier, T. Henstock, S. D. B. Goes, J. M. Kendall, F. Krueger, A. Rietbrock, Seismic Imaging of the Lesser Antilles Subduction Zone Using S-to-P Receiver Functions. *AGU Fall Meet. Abstr.* **53** (2019) (available at http://adsabs.harvard.edu/abs/2019AGUFM.S53C0521C).
48. O. González, V. Clouard, S. Tait, G. F. Panza, S-wave velocities of the lithosphere-asthenosphere system in the Lesser Antilles from the joint inversion of surface wave dispersion and receiver function analysis. *Tectonophysics.* **734–735**, 1–15 (2018).
49. S. Goes, J. Collier, J. Blundy, J. Davidson, N. Harmon, T. Henstock, J. Kendall, C. Macpherson, A. Rietbrock, K. Rychert, Project VoiLA: Volatile recycling in the Lesser Antilles. *Eos.* **100** (2019), doi:10.1029/2019EO117309.
50. H. Kopp, W. Weinzierl, A. Becel, P. Charvis, M. Evain, E. R. Flueh, A. Gailler, A. Galve, A. Hirn, A. Kandilarov, D. Klaeschen, M. Laigle, C. Papenberg, L. Planert, E. Roux, Deep structure of the central Lesser Antilles Island Arc: Relevance for the formation of continental crust. *Earth Planet. Sci. Lett.* **304**, 121–134 (2011).
51. M. Paulatto, M. Laigle, A. Galve, P. Charvis, M. Sapin, G. Bayrakci, M. Evain, H. Kopp, Dehydration of subducting slow-spread oceanic lithosphere in the Lesser Antilles. *Nat. Commun.* **8**, 15980 (2017).
52. I. Jackson, U. H. Faul, Grainsize-sensitive viscoelastic relaxation in olivine: Towards a

robust laboratory-based model for seismological application. *Phys. Earth Planet. Inter.* **183**, 151–163 (2010).
53. C. Havlin, B. K. Holtzman, E. Hopper, Inference of thermodynamic state in the asthenosphere from anelastic properties, with applications to North American upper mantle. *Phys. Earth Planet. Inter.* **314**, 106639 (2021).
54. U. H. Faul, I. Jackson, Transient creep and strain energy dissipation: An experimental perspective. *Annu. Rev. Earth Planet. Sci.* **43**, 541–569 (2015).
55. Y. Takei, Effects of partial melting on seismic velocity and attenuation: A new insight from experiments. *Annu. Rev. Earth Planet. Sci.* **45**, 447–470 (2017).
56. G. A. Abers, P. E. van Keken, B. R. Hacker, The cold and relatively dry nature of mantle forearcs in subduction zones. *Nat. Geosci.* **10**, 333–337 (2017).
57. J. Corbeau, O. Gonzalez, N. Feuillet, A. Lejeune, F. R. Fontaine, V. Clouard, J. Saurel, the OVSM Team, A Significant Increase in Interplate Seismicity near Major Historical Earthquakes Offshore Martinique (FWI). *Bull. Seismol. Soc. Am.* **111**, 3118–3135 (2021).
58. F. Halpaap, S. Rondenay, A. Perrin, S. Goes, L. Ottemöller, H. Austrheim, R. Shaw, T. Eeken, Earthquakes track subduction fluids from slab source to mantle wedge sink. *Sci. Adv.* **5**, eaav7369 (2019).
59. D. Arcay, Dynamics of interplate domain in subduction zones: influence of rheological parameters and subducting plate age. *Solid Earth*. **3**, 467–488 (2012).
60. G. Wadge, Comparison of volcanic production rates and subduction rates in the Lesser Antilles and Central America. *Geology*. **12**, 555–558 (1984).
61. M. Bohm, C. Haberland, G. Asch, Imaging fluid-related subduction processes beneath Central Java (Indonesia) using seismic attenuation tomography. *Tectonophysics*. **590**, 175–188 (2013).
62. T. Chen, R. W. Clayton, Seismic attenuation structure in central Mexico: Image of a focused high-attenuation zone in the mantle wedge. *J. Geophys. Res. Solid Earth*. **114** (2009), doi:10.1029/2008JB005964.
63. E. Hopper, H. A. Ford, K. M. Fischer, V. Lekic, M. J. Fouch, The lithosphere–asthenosphere boundary and the tectonic and magmatic history of the northwestern United States. *Earth Planet. Sci. Lett.* **402**, 69–81 (2014).
64. N. Feuillet, I. Manighetti, P. Tapponnier, E. Jacques, *J. Geophys. Res. Solid Earth*, in press, doi:https://doi.org/10.1029/2001JB000308.
65. Albuquerque Seismological Laboratory (ASL)/USGS, *Caribbean USGS Network* (International Federation of Digital Seismograph Networks, 2006; http://www.fdsn.org/doi/10.7914/SN/CU).
66. Institut De Physique Du Globe De Paris (IPGP), Ecole Et Observatoire Des Sciences De La Terre De Strasbourg (EOST), *GEOSCOPE, French Global Network of broad band seismic stations* (Institut de physique du globe de Paris (IPGP), Université de Paris, 1982; http://geoscope.ipgp.fr/networks/detail/G/).
67. KNMI, *Caribbean Netherlands Seismic Network* (Royal Netherlands Meteorological Institute (KNMI), 2006; http://rdsa.knmi.nl/network/NA/).
68. Institut De Physique Du Globe De Paris (IPGP), *GNSS, seismic broadband and strong motion permanent networks in West Indies* (Institut de physique du globe de Paris (IPGP), Université de Paris, 2008; http://volobsis.ipgp.fr/networks/detail/WI/).
69. S. S. Wei, D. A. Wiens, P-wave attenuation structure of the Lau back-arc basin and implications for mantle wedge processes. *Earth Planet. Sci. Lett.* **502**, 187–199 (2018).
70. K. Aki, P. G. Richards, *Quantitative seismology* (2002).
71. J. G. Anderson, S. E. Hough, A model for the shape of the fourier amplitude spectrum of acceleration at high frequencies. *Bull. Seismol. Soc. Am.* **74**, 1969–1993 (1984).

72. M. Lindner, A. Rietbrock, L. Bie, S. Goes, J. Collier, C. Rychert, N. Harmon, S. P. Hicks, T. Henstock, the V. working group, Bayesian regional moment tensor from ocean bottom seismograms recorded in the Lesser Antilles: Implications for regional stress field (2022), , doi:10.48550/ARXIV.2206.05502.
73. G. A. Prieto, R. L. Parker, F. L. Vernon III, A Fortran 90 library for multitaper spectrum analysis. *Comput. Geosci.* **35**, 1701–1710 (2009).
74. R. Madariaga, Dynamics of an expanding circular fault. *Bull. Seismol. Soc. Am.* **66**, 639–666 (1976).
75. I. Jackson, J. D. F. Gerald, U. H. Faul, B. H. Tan, *J. Geophys. Res. Solid Earth*, in press, doi:https://doi.org/10.1029/2001JB001225.
76. D. Eberhart-Phillips, M. Chadwick, S. Bannister, Three-dimensional attenuation structure of central and southern South Island, New Zealand, from local earthquakes. *J. Geophys. Res. Solid Earth.* **113** (2008).
77. A. Rietbrock, P wave attenuation structure in the fault area of the 1995 Kobe earthquake. *J. Geophys. Res. Solid Earth.* **106**, 4141–4154 (2001).
78. S. P. Hicks, A. Rietbrock, I. M. Ryder, C.-S. Lee, M. Miller, Anatomy of a megathrust: The 2010 M8. 8 Maule, Chile earthquake rupture zone imaged using seismic tomography. *Earth Planet. Sci. Lett.* **405**, 142–155 (2014).
79. F. Crameri, G. E. Shephard, P. J. Heron, The misuse of colour in science communication. *Nat. Commun.* **11**, 5444 (2020).
80. L. Krischer, T. Megies, R. Barsch, M. Beyreuther, T. Lecocq, C. Caudron, J. Wassermann, ObsPy: a bridge for seismology into the scientific Python ecosystem. *Comput. Sci. Discov.* **8**, 014003 (2015).

Acknowledgements

Colour palettes used for making figures in this paper come from the Scientific Colour Maps 6 package (*79*). Figures were plotted with matplotlib and GMT. Seismic data were processed using the ObsPy package (*80*). We thank the German Instrument Pool for Amphibian Seismology (DEPAS), hosted by the Alfred Wegener Institute Bremerhaven, and the Scripps Institution of Oceanography (OBSIP) for providing the ocean-bottom seismometers. We thank the officers and crew of the RRS James Cook, and all volunteers, for their efforts during the ocean bottom seismometer deployment and recovery expedition legs. We are grateful to the University of the West Indies Seismic Research Centre (UWI-SRC) for assisting with the deployment of temporary land stations.

Funding

Natural Environment Research Council (NERC) Large Grant, with the following grant numbers NE/K010654/1 (SPH, CAR, NH, TH); NE/K010743/1 (SG, JSC, JJW). NE/K010611/1 (LB, AR), NE/K010824/1 (GC, CM), NE/K010662/1 (JDB).

National Science Foundation grant 2042553 (SSW).

Author contributions

Conceptualization: SPH, CAR, NH, SG, AR, JSC, TJH, CM, JJW, JB, JMK.
Methodology: SPH, LB, CAR, NH, SG, AR, SSW.
Software: SPH, CAR, NH, SSW, AR.
Formal analysis: SPH, NH, LB, SG.
Investigation: SPH, LB, NH, AR, JSC, TJH, LL, GFC.
Writing - original draft: SPH, LB, CAR, NH, SG.
Writing - review & editing: SPH, LB, CAR, NH, SG, AR, SSW, JSC, TJH, LL, JP, CM, DS, JJW, GFC, JB, JMK.

VoiLA Working Group

Jeroen van Hunen & Jon Davidson (Durham Univ.), Marjorie Wilson (Univ. Leeds), Robert Allen & Benjamin Maunder (Imperial College London), Ben Chichester (Univ. Southampton), Steve Tait (Institut de Physique du Globe de Paris), Richard Robertson & Joan Latchman (Seismic Research Centre, Univ. West Indies), Frank Krüger (Univ. Potsdam).

Competing interests

The authors declare that they have no competing interests.

Data and materials availability

Our spectral inversion t^* dataset and the resulting 3-D attenuation tomography models can be found at the following repository: https://doi.org/10.5281/zenodo.6822900.